



# Flight stability of wedges

Pejman Sanaei<sup>a,b</sup>, Guanhua Sun<sup>a</sup>, Huilin Li<sup>a,c</sup>, Charles S. Peskin<sup>a</sup>,  
Leif Ristroph<sup>a,\*</sup>

<sup>a</sup> Courant Institute of Mathematical Sciences and Department of Mathematics, New York University, New York, NY 10012, United States of America

<sup>b</sup> Department of Mathematics, New York Institute of Technology, New York, NY 10023, United States of America

<sup>c</sup> Department of Mathematics, NYU Shanghai, Shanghai, 200122, China

## ARTICLE INFO

### Article history:

Received 11 June 2020

Received in revised form 14 December 2020

Accepted 6 January 2021

Available online 23 January 2021

### Keywords:

Fluid–structure interaction

Flight stability

Immersed boundary method

Oriental stability

Postural stability

## ABSTRACT

Recent experiments have shown that cones of intermediate apex angles display orientational stability with apex leading in flight. Here we show in experiments and simulations that analogous results hold in the two-dimensional context of solid wedges or triangular prisms in planar flows at Reynolds numbers  $Re \sim 10^2$  to  $10^3$ . Slender wedges are statically unstable with apex leading and tend to flip over or tumble, and broad wedges oscillate or flutter due to dynamical instabilities, but those of apex half angles between about  $40^\circ$  and  $55^\circ$  maintain stable posture during flight. The existence of “Goldilocks” shapes that possess the “just right” angularity for flight stability is thus robust to dimensionality. We also show that the stability is robust to moderate changes in shape and Reynolds number.

© 2021 Elsevier Ltd. All rights reserved.

## 1. Introduction

The flight stability of an object is a fundamental fluid–structure interaction problem. Whether a falling leaf or a powered airplane, the orientation or posture of the body is coupled to its free motions via aerodynamic torques (Pesavento and Wang, 2004; Abzug and Larrabee, 2005). Because of its importance in many technologies and prevalence in everyday life, this problem has invited many strategies for achieving straight or oriented flight in which rotations are suppressed. The flight stability of darts, arrows, kites, rockets, missiles and other projectiles is ensured by the addition of aerodynamic surfaces such as feathers, fins, and tails (Murphy, 1981). Center of mass position also plays a central role in stability, as illustrated by parachutes, paper airplanes and all forms of aircraft (Abzug and Larrabee, 2005; Kim and Peskin, 2006, 2009). Other strategies include inducing spin of an object for gyroscopic stabilization, as in the flight of frisbees, boomerangs and bullets (Lorenz, 2007). The overall shape of an object, which factors into its mass and fluid force/torque distributions, is another major determinant of stability.

Very recently, a particularly simple form of flight stability based purely on shape was discovered experimentally for solid cones of homogeneous density, without additional surfaces and without spin (Amin et al., 2019). Laboratory experiments on cones falling through water at Reynolds numbers  $10^3$  to  $10^4$  show that, while slender cones flip over or tumble and broad cones flutter back and forth, those of intermediate apex half angles  $\alpha \in [30^\circ, 50^\circ]$  maintain apex-leading orientation during flight. This observation has recently been confirmed in independent experiments (Kim et al., 2020). The study by Amin et al. was motivated by so-called oriented meteorites (Amin et al., 2019), whose conical shapes strongly

\* Corresponding author.

E-mail addresses: [psanaei@nyit.edu](mailto:psanaei@nyit.edu) (P. Sanaei), [ristroph@cims.nyu.edu](mailto:ristroph@cims.nyu.edu) (L. Ristroph).

suggest fixed posture during flight through the atmosphere, during which the meteoroid is carved and reshaped by the extreme aerodynamic heating and ablation (Norton, 2002). It is argued that these particular cone shapes survive the flight and arrive on Earth as such because of their stability, whereas other shapes tumble, ablate more isotropically and arrive as the “blobby” forms more typical of meteorites. Interestingly, conical meteorites have half angles of about  $40^\circ$  to  $50^\circ$ , which falls within the angular range for stable flight in experiments (Amin et al., 2019). However, this correspondence should be viewed as coincidental, since the hypersonic flight of meteoroids is vastly different from the conditions explored at laboratory scales.

Nonetheless, the clear demonstration of oriented flight is intriguing given the predominance of unsteady modes such as tumbling and fluttering for simple shapes such as plates, disks, cylinders and spheres moving at comparable Reynolds numbers (Willmarth et al., 1964; Jayaweera and Mason, 1965; Smith, 1971; Field et al., 1997; Pesavento and Wang, 2004; Andersen et al., 2005; Ern et al., 2012). Cones of intermediate breadth thus stand out as “straight shooters” (Amin et al., 2019), and their oriented flight motivates many questions about the flow–structure interaction physics. What is the fluid dynamical mechanism behind the stabilization? How is pressure redistributed to ensure restoring torques in response to changes in orientation, and how are rotations damped? Can the phenomenon of oriented flight be reproduced and validated in simulations and/or models? How robust is the phenomenon to dimensionality (*i.e.* 2D versus 3D), Reynolds number, and details of the shape?

The goal of this work is to address some of these questions in the two-dimensional context of wedges or triangular prisms in planar flows at moderately high Reynolds numbers. The family of wedges of varying apex angles spans shapes from slender or sharp to broad or dull, and flow past these objects is a canonical context considered in many fluid dynamics studies. Flow impinging on a wedge of infinite extent is a classic calculation in the theories of potential flow and boundary layers (Schlichting and Gersten, 2016). The flight of a finite wedge, however, is expected to involve flow separation, wake formation and consequent modifications to the flow and pressure fields over the entire surface. While many studies have assessed flow characteristics for fixed finite-size wedges (Liepmann and Bryson, 1950; Acrivos et al., 1968; El-Sherbiny, 1983; Kumar De and Dalal, 2006; Camarri et al., 2006; Prasath et al., 2014), relatively few have considered free motions, dynamical modes, and flight stability (Tatsuno et al., 1990; Skews, 1991; Wang et al., 2011). Most importantly, missing from the literature seems to be a systematic characterization of flight stability across the family of wedges.

Here, we conduct experiments and simulations aimed at understanding the static stability of body orientation or posture for wedges in flows at Reynolds numbers  $10^2$  to  $10^3$ . We also carry out free flight experiments that uncover dynamic stability properties, and we explore shapes beyond wedges in order to assess the robustness of our observations. Taken together, our findings establish the generality of the “Goldilocks” rule-of-thumb that only shapes of the “just right” angularity – neither too slender nor overly broad – are stable in flight.

## 2. Dynamic stability: Free flight experiments

We first investigate the *dynamic stability* or free flight behavior of wedge shapes through experiments on solid bodies released to fall through water under gravity. To achieve quasi-2D wedges, we 3D-print from plastic triangular prisms whose depth or height (15 cm) is much greater than the centimeter-scale dimensions of the cross-section. The cross-section takes the form of an isosceles triangle, with an apex or vertex half angle of  $\alpha$  and the other two angles being equal, as shown in Fig. 1(e). Each object is released in a large water tank ( $30 \times 30 \times 60$  cm in length, width and height respectively) and the flight trajectories captured by long-exposure-time photographs taken under stroboscopic lighting. The example photographs of Fig. 1 show the flight positions and postures at 1/10-s intervals for different wedges. In all cases, the body is released from rest and with the apex aimed downward, and each image represents later times after a terminal flight mode is attained.

Before discussing the observed modes, we note the relevant scales, forces and fluid dynamical regime. The solid bodies have characteristic length  $L = \sqrt{A} = 1.6$  cm set by the cross-section area  $A = 2.5$  cm<sup>2</sup>, which is fixed across all wedges. The solid density is  $\rho_s = 1.2$  g/cm<sup>3</sup>, and the fluid parameters are the density  $\rho_f = 1.0$  g/cm<sup>3</sup> and dynamic viscosity  $\mu = 10^{-2}$  g/cm·s of water, which combine to form the kinematic viscosity  $\nu = \mu/\rho_f = 10^{-2}$  cm<sup>2</sup>/s. Considering per-unit-span forces, we may balance buoyancy-adjusted weight  $(\rho_s - \rho_f)gL^2$  against high-Reynolds-number pressure drag  $\rho_f U^2 L$  to estimate the speed scale (Tritton, 2012; Amin et al., 2019):  $U \sim \sqrt{(\rho_s/\rho_f - 1)gL} = 18$  cm/s, where  $g = 980$  cm/s<sup>2</sup> is gravitational acceleration. The resulting Reynolds number  $Re = UL/\nu \sim 2900$  is high, indicating the dominance of inertial over viscous fluid forces. (Note that this definition of  $Re$  is closely related to the Archimedes number (Ern et al., 2012):  $Ar = \rho_f(\rho_s - \rho_f)gL^3/\mu^2 = Re^2$ .) We refine this estimate by directly measuring from the stroboscopic images the average terminal descent speeds across  $\alpha \in [10^\circ, 70^\circ]$ . The values lie within  $U = 15 \pm 2$  cm/s, corresponding to Reynolds numbers of  $Re = 2400 \pm 300$ . Hence  $Re$  does not differ significantly across the bodies studied here.

These experiments reveal four distinct flight behaviors that are attained by changing the apex half angle  $\alpha$ . For sufficiently slender or sharp wedges of  $\alpha \lesssim 20^\circ$ , the body quickly inverts or flips over so that its apex is aimed upward, and then descends while oscillating strongly in orientation about this apex-up posture. A representative example of this *inverted fluttering* behavior is shown in Fig. 1(a) for the case of  $\alpha = 15^\circ$ . For somewhat broader wedges of  $25^\circ \lesssim \alpha \lesssim 35^\circ$ , the body descends at an angle while continuously spinning with a fixed sense of rotation. An example of such *tumbling* is seen in Fig. 1(b) for an equilateral triangle of  $\alpha = 30^\circ$ . Yet broader wedges of  $40^\circ \lesssim \alpha \lesssim 55^\circ$  are seen to maintain apex-downward orientation while descending, and this *oriented flight* is shown in Fig. 1(c) for  $\alpha = 45^\circ$ . Finally, very broad

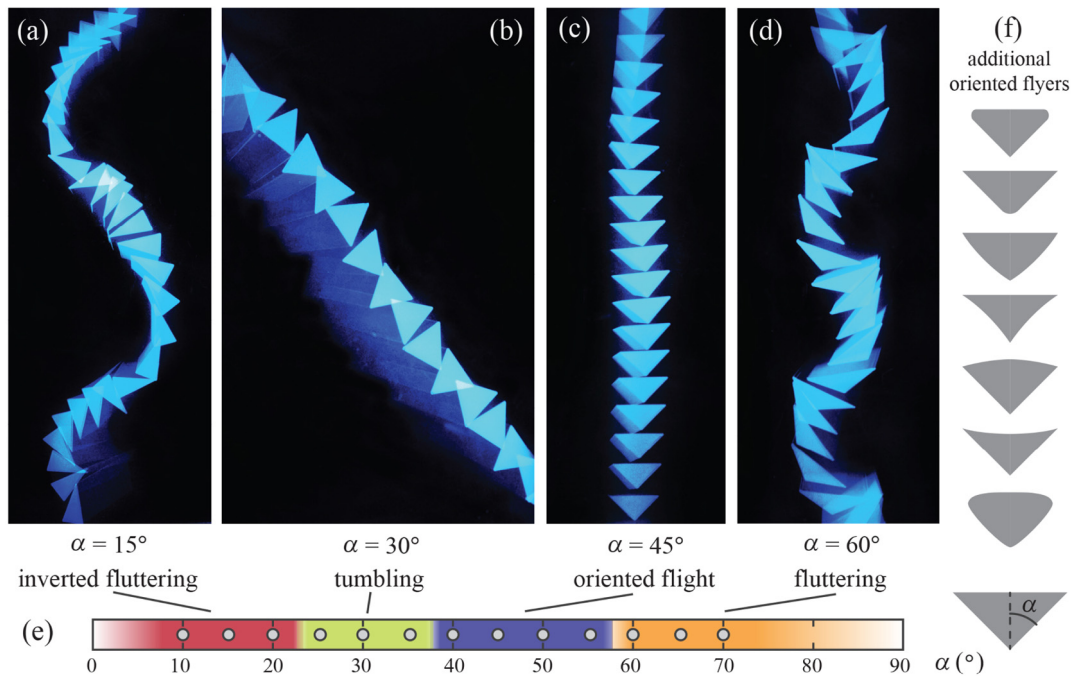


**Fig. 1.** Free flight modes of triangular prisms of varying apex half angle  $\alpha$ . (a–d) Photographs taken under stroboscopic lighting capture the descent and rotations of 3D-printed prisms falling within water. The selected bodies of  $\alpha = 15^\circ$ ,  $30^\circ$ ,  $45^\circ$  and  $60^\circ$  display the characteristic behaviors of inverted fluttering, tumbling, oriented flight and fluttering. (e) Diagram of how flight modes vary with  $\alpha$ . Circles represent all prisms tested in this study, and modes are color coded. (f) Additional shapes that display oriented flight in experiments. These cross-sections represent simple perturbations to a wedge of  $\alpha = 45^\circ$ . (For interpretation of the references to color in this figure legend, the reader is referred to the web version of this article.)

shapes of  $\alpha \gtrsim 60^\circ$  oscillate strongly about the apex-downward posture, and an example of such *fluttering* is shown in Fig. 1(d) for  $\alpha = 60^\circ$ .

The above classifications deserve some justification based on observations. The oscillatory modes of inverted fluttering and fluttering are distinguished by the mean posture about which the body oscillates, which is apex-up (to be indicated as  $\theta = 180^\circ$  in following sections) for the former and apex-down ( $\theta = 0^\circ$ ) for the latter. We interpret oriented flight, while subject to slight postural fluctuations, as distinct from fluttering for several reasons. First, rotation amplitudes are typically less than  $5^\circ$ , far smaller than the excursions beyond  $45^\circ$  observed for fluttering. Further, the transition from oriented flight to fluttering seems to be abrupt: All bodies of  $\alpha \in [40^\circ, 55^\circ]$  display uniformly small excursions, whereas all bodies of  $\alpha \geq 60^\circ$  undergo large amplitude oscillations. Finally, the slight rotations during oriented flight are not periodic and vary trial to trial, whereas the fluttering motions are strongly periodic and highly repeatable. These characteristics distinguishing oriented flight from fluttering have also been observed in the study of Amin et al. on cones (Amin et al., 2019), from which we adopt the terminology.

The relationship between shape, as specified by  $\alpha$ , and free flight behavior is summarized by the colored map of Fig. 1(e). Here the markers represent the specific wedges tested in experiments, and the color assigns the most prevalent flight mode observed over many trials. These data confirm that stably oriented flight is achieved only for wedges of intermediate apex angles  $\alpha \in [40^\circ, 55^\circ]$ .

It is interesting to ask whether this stability is sensitive to aspects of shape beyond angularity of the front surface. To test this experimentally, we 3D-print bodies whose cross-sections represent simple perturbations to a wedge of  $\alpha = 45^\circ$ , which is an oriented flyer. In Fig. 1(f) we show seven additional bodies formed by rounding corners and/or introducing concavity or convexity to the edges, with perturbations done so as to preserve left–right symmetry. These modifications are combined in the final body shown, which has been chosen to resemble the characteristic shape formed by fluid mechanical erosion (Ristroph et al., 2012; Moore et al., 2013). Remarkably, all of these bodies display oriented flight. This suggests that, in some general sense, it is the specific angularity of the front surface that imparts stability, with other details of the shape playing a lesser role.

### 3. Static stability: Torque response in experiments and simulations

To gain insight into the observed free flight behaviors, we next carry out systematic studies of the fluidic torque response for changes in orientation of wedges fixed within imposed flows. We carry out such *static stability* tests in both

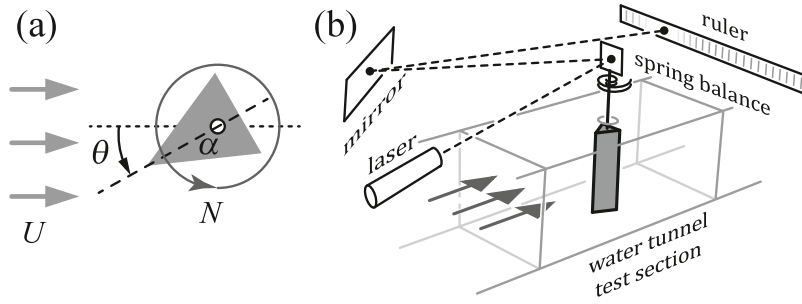


**Fig. 2.** Schematics representing static stability tests and experimental apparatus. (a) Idealized 2D problem of a triangular wedge of apex half angle  $\alpha$  and orientation  $\theta$  relative to a flow of speed  $U$ . The flow exerts a torque  $N$  about the center of mass. (b) Spring balance apparatus for measuring torque on a triangular prism in the flow of a water tunnel. Fluidic torques load a torsion spring and induce slight rotations that are amplified for measurement. Not shown is a viscous dashpot that sits atop the mounting shaft and suppresses fluctuations caused by unsteady torques.

water tunnel experiments and immersed boundary computational fluid dynamics simulations. We also use these results to identify stable and unstable postures across the family of wedges, as well as a potential that quantifies the degree of stabilization.

### 3.1. Experimental methods

We first carry out torque-versus-orientation measurements for wedges of varying apex half angle  $\alpha$  fixed within the flow of a water tunnel. Similar to the quasi-2D situation of the free flight tests, each body is a 3D-printed solid triangular prism whose length (14.5 cm) is much greater than the centimeter-scale dimensions of the cross-section, which is an isosceles triangle of apex half angle  $\alpha$  [Fig. 2(a)]. As shown in Fig. 2(b), the body is mounted upright to the vertical shaft of a Cavendish-style torsion spring balance (Alben et al., 2002; Ristroph and Zhang, 2008; Amin et al., 2019). The balance sits atop the test section (15 × 15 cm in cross-section and 50 cm in length) of a laminar flow water tunnel (Engineering Laboratory Designs, Inc.). The body may be fixed at any orientation angle  $\theta$  relative to the incoming water flow, where  $\theta = 0^\circ$  corresponds to the apex aimed directly into the flow. The torque exerted on the body by the flow loads the spring and slightly rotates the body ( $< 2^\circ$  for the conditions studied here). By mounting through the center of mass, which is 1/3 from the base to the apex for all solid wedges, we ensure that these rotations reflect only fluid dynamical torques about this point.

The slight rotations of the body along with its mounting shaft are amplified for measurement by reflecting a laser beam off a small mirror affixed to the top of the shaft, as shown in Fig. 2(b). The reflected beam impinges on a ruler via a long path – achieved compactly with a second mirror – which ensures that small rotations lead to measurably large displacements on the ruler. Torque–displacement calibration is then carried out via a string–mass–pulley system, which leads to a conversion factor of 4.64 dyn · cm per mm (Amin et al., 2019). By systematically sweeping through orientations for a given body and selected flow speed  $U$  and measuring the corresponding displacements, we build a profile of torque  $N$  versus orientation angle  $\theta$ . Systematically varying the body shape, as specified by the apex angle  $\alpha$ , then leads to a complete characterization of static stability across the family of wedges.

While simple and direct, the spring balance system can be made exquisitely sensitive and care must be taken to ensure reliable operation. Our procedures build on past experiences with similar devices (Ristroph and Zhang, 2008) and especially the work of Amin et al. (2019), the same apparatus being employed here. High quality components are used for the moving elements that are most critical to its performance, including ultra-low friction, stainless steel ball bearings on which the mounting shaft rotates and a precision spring steel coil that serves as the torsion spring. These parts sit above the tunnel test section and are never in contact with water, and the entire setup is in a laboratory space with standard climate control that maintains temperature and humidity. While the readout is done by visually recording the location of the laser point along a long ruler, the precision is made possible by the extreme amplification of the rotation due to the long travel path of the beam. The dimensions of our system are such that rotations on the order of a degree lead to beam displacements of about a meter. The beam spot itself measures a few millimeters in radius, so the system has high dynamic range. Undesirable oscillations of the body due to fluctuations in the hydrodynamic torque (e.g. vortex shedding) are suppressed by a viscous dashpot that is mounted to the top of the shaft. This damper consists of an outer cylinder secured to the shaft and an inner, concentric cylinder fixed in the lab, with high viscosity silicone oil (10,000 cP) between the two. When the body is loaded by an imposed flow, the system typically takes on the order of 10 s to reach an equilibrium posture, about which it oscillates with exceedingly small amplitude. These oscillations contribute to the experimental errors, which measure about 1% and are characterized in detail below.

We report on results for ten wedges that span all four free flight modes discussed above. Specifically, we consider apex half angles  $\alpha \in [15^\circ, 60^\circ]$  in  $5^\circ$  increments. The height or span of all wedges are 14.5 cm, which ensures they extend across the 15-cm height of the tunnel without contacting the top or bottom. The longest dimension of the cross-section,

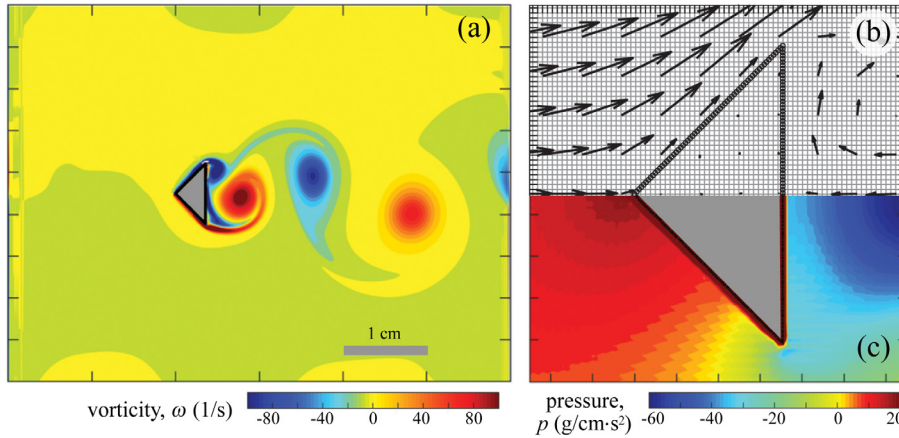


**Fig. 3.** Computational fluid dynamics simulations via the Immersed Boundary Method. (a) Snapshot of the computed vorticity field at Reynolds number  $Re = 200$  for a triangle of apex half angle  $\alpha = 45^\circ$ . The region displayed represents the entire computational domain, with periodic boundary conditions on the upper and lower walls and imposed uniform velocity over the left (entry) and right (exit) walls. (b) Zoomed-in view showing time-averaged flow velocity vectors as well as the computational grid. (c) Time-averaged pressure field map. (For interpretation of the references to color in this figure legend, the reader is referred to the web version of this article.)

i.e. either the base width or height, is set to be 2.5 cm, which ensures that any body at any orientation has a filling area fraction of no more than 16%. The speeds are selected to achieve Reynolds numbers  $Re \sim 10^3$  similar to the free flight case. The specific values of  $U = 9.1$  cm/s for  $\alpha = 15^\circ - 25^\circ$  and  $U = 13.7$  cm/s for  $\alpha = 30^\circ - 60^\circ$  were selected based on convenience given the observed range of laser beam displacements along the ruler. These speeds along with the length scales of  $L = \sqrt{A} = 1.0$  to 1.7 cm for the various bodies tested yield  $Re = 1700 \pm 500$ .

### 3.2. Simulation methods

We next implement computational fluid dynamics simulations of the flow around triangles using the Immersed Boundary Method (IBM) in order to extract torque-orientation profiles. A snapshot in time of the flow vorticity throughout the computational domain is shown in Fig. 3(a), and magnified views near the body of the time-averaged velocity and pressure fields are shown in Figs. 3(b) and (c). The method describes the solid structure with Lagrangian or co-moving coordinates and the fluid with Eulerian or ‘lab frame’ coordinates, where the forces of interaction between the two are communicated locally in a manner consistent with Newton’s laws (Peskin, 1972; McQueen and Peskin, 1997; Arthurs et al., 1998; Lai and Peskin, 2000; Griffith et al., 2009; Balboa et al., 2011; Devendran and Peskin, 2012; IBAMR, 0000). For the rigid and fixed bodies considered here, we adopt the Penalty Immersed Boundary Method (Kim and Peskin, 2016), which introduces a third set of *tether points* that are absolutely fixed in space and represent the desired shape and location of the solid boundary. The solid boundary points are connected to the tether points via springs, and it is only the solid boundary points that interact with the fluid. Stiff springs approximate a rigid boundary, at the cost of numerical stiffness but with the benefit of ease of implementation. In practice, accurate results can be achieved with appropriate choices of spring constant, spatial discretization, time-stepping and other numerical parameters (Kim and Peskin, 2016). Results from spatial and temporal convergence tests are presented in a later section.

The continuum form of the coupled fluid–solid dynamical equations are:

$$\rho \left( \frac{\partial \mathbf{u}}{\partial t} + \mathbf{u} \cdot \nabla \mathbf{u} \right) = -\nabla p + \mu \Delta \mathbf{u} + \mathbf{f}, \quad \nabla \cdot \mathbf{u} = 0, \quad (1)$$

$$\mathbf{f}(\mathbf{x}, t) = \int \mathbf{F}(s, t) \delta(\mathbf{x} - \mathbf{X}(s, t)) ds, \quad (2)$$

$$\frac{\partial \mathbf{X}}{\partial t}(s, t) = \mathbf{U}(\mathbf{X}(s, t), t) = \int \mathbf{u}(\mathbf{x}, t) \delta(\mathbf{x} - \mathbf{X}(s, t)) d\mathbf{x}, \quad (3)$$

$$\mathbf{F}(s, t) = -k(\mathbf{X}(s, t) - \mathbf{Z}(s, t)). \quad (4)$$

Here  $\rho$  and  $\mu$  are the density and viscosity of the fluid and  $k$  is a spring constant;  $\mathbf{x}$  and  $\mathbf{X}$  are the Eulerian fluid coordinate and the Lagrangian boundary coordinate;  $\mathbf{u}(\mathbf{x}, t)$  and  $\mathbf{U}(\mathbf{X}(s, t), t)$  represent the fluid and solid velocities;  $\mathbf{f}$  and  $\mathbf{F}$  are the Eulerian and the Lagrangian force densities; and  $\delta$  is a 2D delta function. Eq. (1) is the Navier–Stokes equation describing incompressible flow of a viscous fluid. Eq. (2) describes how force is imparted from the boundary to the fluid. Eq. (3) ensures the boundary moves with the local flow field, which enforces the no-slip boundary condition. Eq. (4) describes

**Table 1**  
Parameter definitions and values used in the simulations.

Parameter	Formula and description	Typical value	Units
$\rho$	Fluid density	1	g/cm <sup>3</sup>
$\mu$	Fluid viscosity	0.01	g/(cm s)
$k$	Spring constant	1 000 000	g/s <sup>2</sup>
$h$	Fluid mesh width	0.0117	cm
$h_b$	Boundary mesh width	0.0078	cm
$L_x$	Domain length	6	cm
$L_y$	Domain width	4.5	cm
$N_x$	Streamwise grid resolution	512	
$N_y$	Lateral grid resolution	384	
$L$	Side length of the triangle	0.5	cm
Re	Reynolds Number	200	
$U$	Flow speed	5	cm/s
$\Delta t$	Time step	0.0001	s
$T$	Simulation time	8	s

the tether-point construction and the associated spring force on the solid boundary. Here,  $\mathbf{Z}$  and  $\mathbf{X}$  are the locations of tether and solid boundary points, respectively.

The continuum formalism described above is then implemented in simulations that build on the work of Kim & Peskin to solve the coupled equations discretized in space and numerically integrated in time (Kim and Peskin, 2016). Briefly, we employ a fixed square grid for the fluid, a fixed boundary mesh for the solid, and a fixed time step in a second-order Runge–Kutta scheme. The delta function is also discretized and distributed over four adjacent points. Simulation parameter values are given in Table 1. The physical constants pertaining to the fluid material parameters, body scale and flow speed are chosen to correspond to water flow at moderately high Reynolds numbers of  $Re = 100$  to  $300$ . (Higher  $Re$  values require significantly longer run times to achieve similarly accurate results.) Periodic boundary conditions are imposed on the bottom and top walls, and the horizontal flow velocity is imposed to be uniform over the entire entry (left wall) and exit (right wall). These conditions are expected to better approximate open flow for larger domains, and our domain size was selected following a sensitivity analysis.

Running the simulation furnishes solutions to all flow and boundary quantities of interest. Here, we focus on the total torque exerted on the body. The instantaneous torque may be extracted via a discrete sum of forces over the solid boundary:

$$N(t) = \sum_s \mathbf{r}(s) \times [\mathbf{F}(s, t)h_b], \quad (5)$$

where  $\mathbf{F}(s, t)$  is the Lagrangian force density (force per unit length),  $h_b$  is the mesh width on the boundary, and  $\mathbf{r}(s)$  is the positional vector of each boundary point with respect to the center of mass (location  $1/3$  from base to apex). Simulations are run for 13 wedges of  $\alpha \in [10^\circ, 70^\circ]$  in  $5^\circ$  increments. For each, the wedge is varied over 37 distinct orientations  $\theta \in [0^\circ, 180^\circ]$  in  $5^\circ$  increments, leading to 481 conditions tested in total. The torque is extracted and averaged over later times in order to capture the steady-state behavior.

### 3.3. Torque-versus-orientation profiles

Here, we present static stability or torque-versus-orientation results from experiments and simulations. To facilitate comparison, we first form the torque coefficient  $C_N$ , which normalizes  $N$  for any given wedge  $\alpha$  at any given angle  $\theta$  by removing the effects of fluid density  $\rho_f$ , flow speed  $U$ , and body size based on the known scaling of high- $Re$  pressure forces (Tritton, 2012). For the quasi-2D (but truly 3D) experiments, we define  $C_N = \frac{N}{\frac{1}{2}\rho_f U^2 V}$ , where  $V$  is the volume of the solid. This choice of size scale ensures that  $C_N$  is dimensionless and in effect reveals the torque dependence for wedges or triangular prisms of equal volume (Amin et al., 2019). An analogous normalization can be applied in the truly 2D simulations, taking care to note that fluid density  $\rho$  is the areal density or mass per unit area:  $C_N = \frac{N}{\frac{1}{2}\rho U^2 A}$ , where  $A$  is the area of the triangle.

Figs. 4(a) and (c) show the torque coefficient  $C_N$  versus the orientation angle  $\theta$  for all experiments and simulations, respectively. The general shape of each  $C_N(\theta)$  curve for a given  $\alpha$  is seen to correspond quite well between the two methods, and the general trends for changing  $\alpha$  are also successfully reproduced. Not all quantitative details are well matched, and these differences may be attributed to differences in Reynolds numbers for experiments ( $Re = 1200$  to  $2200$ ) and simulations ( $Re = 100$  to  $300$ ), as well as 3D flow effects (especially at the ends of wedges) in experiments. Both of these factors are expected to yield higher torque coefficients in simulations than experiments, as is borne out by a close comparison of the data. Nonetheless, the strong similarities in qualitative trends indicate that the methods may together offer a common picture of the static stability of wedges.

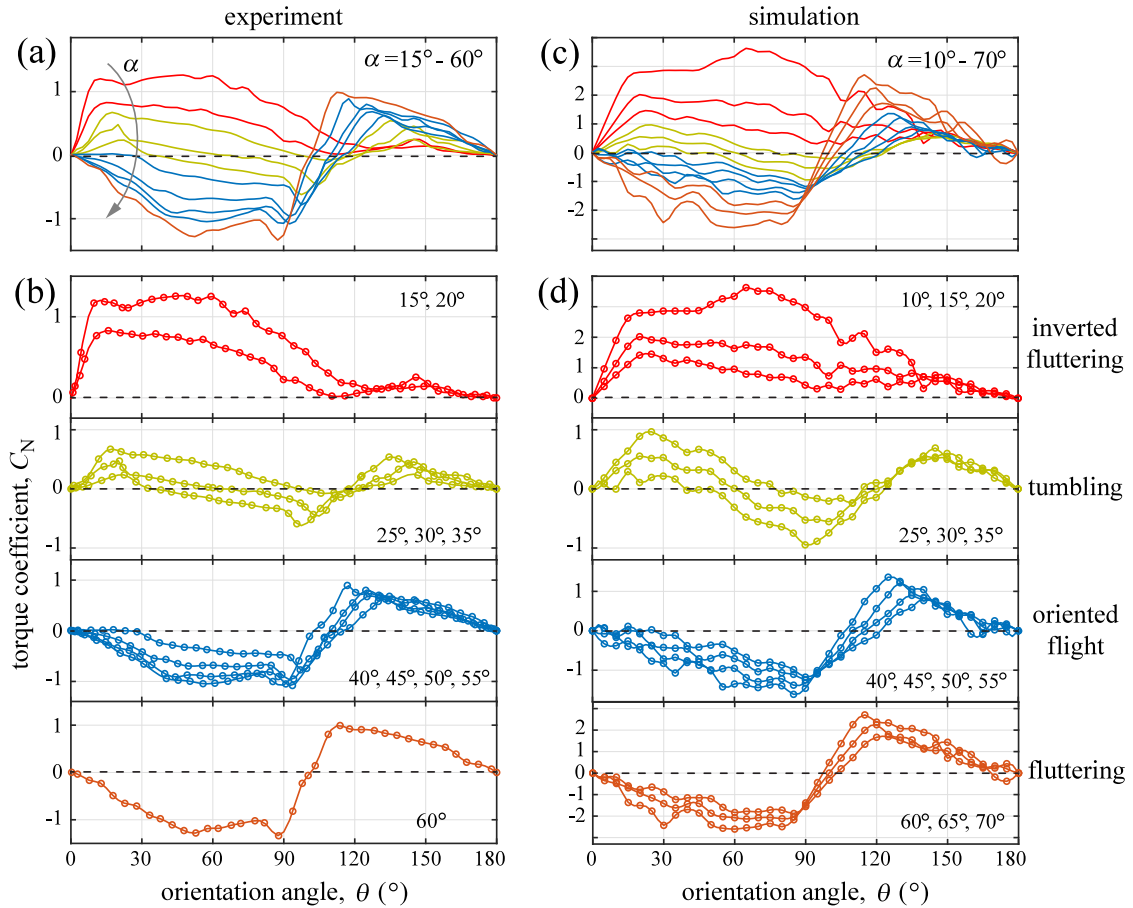


**Fig. 4.** Static stability characterization in experiments and simulations. Curves of the torque coefficient  $C_N$  versus orientation angle  $\theta$  are shown across the family of wedges of varying apex half angle  $\alpha$ . (a) All experimental measurements for  $\alpha = 15^\circ - 60^\circ$ . (b) Experimental measurements broken down by the free flight modes inverted fluttering (red), tumbling (yellow-green), oriented flight (blue) and fluttering (orange). (c) All simulation results for  $\alpha = 10^\circ - 70^\circ$ . (d) Simulations results broken down by flight modes. (For interpretation of the references to color in this figure legend, the reader is referred to the web version of this article.)

### 3.4. Analysis of experimental errors and computational convergence

Before interpreting these results in greater depth, we briefly characterize the errors in the experimental measurements and the convergence characteristics of the simulations. In Fig. 5, we display experimental error bands for the measured torque coefficient across orientation angles  $\theta$  and for selected wedges of half angles  $\alpha = 15^\circ, 30^\circ, 45^\circ$  and  $60^\circ$ , which are representative of the four free flight modes. For each  $\alpha$  and each  $\theta$ , the error is based on repeated measurements of the amplitude of fluctuations in time of the laser beam displacement, appropriately converted to torque coefficient  $C_N$ . The mean absolute errors of 0.01 yield relative errors on the order of 1%, which speaks to the reproducibility of the experimental measurements.

To assess the accuracy of the computations, we carry out convergence studies by running additional simulations for different spatial grids and different values of the integration time step. In Fig. 6(a), we compare the torque-orientation profiles for four example wedges and for three different resolutions of the spatial grid, as quantified by the number of grid cells  $N_x$  in the streamwise dimension. Here,  $N_x = 512$  applies to the results reported throughout this study, and twice coarser and twice finer grids are included for comparison. (The lateral dimension is made proportionally coarser and finer, respectively, preserving the square mesh and 4:3 aspect ratio of the domain.) While the coarser grid of  $N_x = 256$  can lead to significant differences in the computed torque, the selected resolution of  $N_x = 512$  shows good agreement with the finer case of  $N_x = 1024$ . The mean of the absolute differences in  $C_N$  between the latter cases is 0.1, and the associated relative errors of 5% can be taken as a measure of the accuracy of the computations. Similarly, in Fig. 6(b), we show how the integration time step  $\Delta t$  affects the torque profiles. Here the selected value of  $\Delta t = 1.0 \times 10^{-4}$  s yields torque profiles in good agreement with simulations at finer temporal resolution, with typical deviations measuring 0.1 or 5%. Importantly, these tests show that the simulations are sufficiently resolved to distinguish the torque characteristics across wedges of different  $\alpha$ .

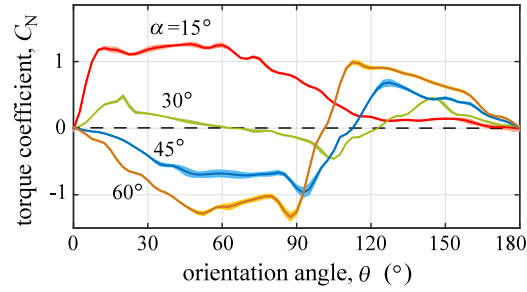


**Fig. 5.** Characterization of errors in experimental torque measurements. Torque-orientation profiles are shown for four example wedges of half angles  $\alpha = 15^\circ, 30^\circ, 45^\circ$  and  $60^\circ$ . The colored band surrounding each curve reflects the amplitude of torque fluctuations in time. (For interpretation of the references to color in this figure legend, the reader is referred to the web version of this article.)

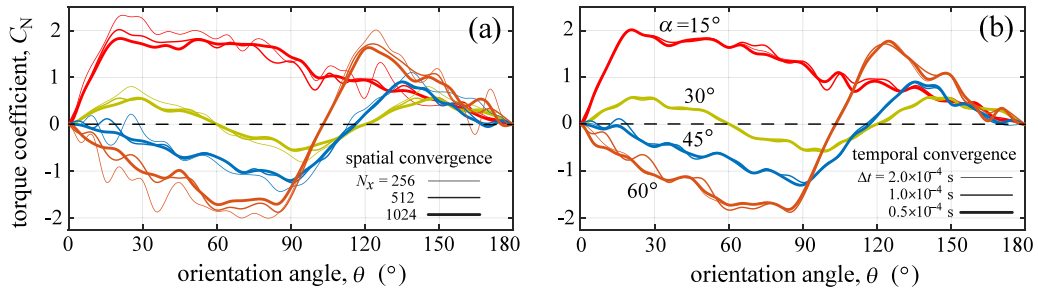


**Fig. 6.** Simulation results for different spatial and temporal discretizations and for selected wedges of half angles  $\alpha = 15^\circ, 30^\circ, 45^\circ$  and  $60^\circ$ . (a) Thicker lines indicate finer spatial discretization, as quantified by the streamwise grid resolution  $N_x$  of the fluid domain. (b) Thicker lines indicate finer temporal discretization, as quantified by the integration time step  $\Delta t$ . The intermediate values  $N_x = 512$  and  $\Delta t = 1.0 \times 10^{-4}$  s are used throughout this work, and the results show good agreement with more finely resolved simulations. (For interpretation of the references to color in this figure legend, the reader is referred to the web version of this article.)

### 3.5. Equilibrium postures and their stability

The equilibrium postures for any given body correspond to values of  $\theta$  for which  $C_N = 0$ . It is readily seen that, for all  $\alpha$  in both experiment and simulation, equilibria exist for  $\theta = 0^\circ$  and  $\theta = 180^\circ$ . These are the trivial zero-torque orientations expected by symmetry when the apex is aimed forward into the flow and backward away from the flow, respectively. Nontrivial equilibria exist for some bodies, as discussed in more detail below.

The static stability of any equilibrium posture can be inferred from the slope  $dC_N/d\theta$ . Positive slope indicates that perturbations in  $\theta$  are amplified and thus unstable, while negative slopes indicate restoring or stabilizing torques. For example, the plots of Figs. 4(a) and (c) show that the stability of the apex-leading equilibrium orientation  $\theta = 0^\circ$  changes with  $\alpha$ . Sharp wedges of smaller  $\alpha$  have positive slope and are thus unstable when aimed into a flow, while wedges of larger  $\alpha$  have negative slopes that imply static stability.

How the equilibria and their stability depend on wedge shape  $\alpha$  can be more clearly seen by separating the  $C_N(\theta)$  curves according to the free flight modes observed in Section 2. In Figs. 4(b) and (d), we show the experimental and simulation data for the modes of inverted fluttering (red), tumbling (yellow-green), oriented flight (blue) and fluttering (orange), where the color coding follows that of Fig. 1(e).

The slender wedges of  $\alpha \lesssim 20^\circ$  that display inverted fluttering during free fall have positive  $C_N$  for all orientations  $0^\circ < \theta < 180^\circ$ , meaning that the only equilibrium postures are the trivial ones  $\theta = 0^\circ$  and  $\theta = 180^\circ$ . Only the latter is stable, which is consistent with these bodies inverting in free flight. For the somewhat broader wedges of  $25^\circ \lesssim \alpha \lesssim 35^\circ$  that tumble, there exist 4 equilibria in total, including a nontrivial stable–unstable pair in addition to the trivial pair. The uniformly low values of  $C_N$  across varying  $\theta$  seem consistent with these bodies tumbling, thereby ‘visiting’ many orientations. Yet broader wedges of  $40^\circ \lesssim \alpha \lesssim 55^\circ$  that display oriented flight have 3 equilibria, where the loss of one equilibrium is accompanied by a change from unstable to stable of the apex-leading posture  $\theta = 0^\circ$ . This stability is consistent with the oriented flight observed in experiments. Finally, the very broad shapes of  $\alpha \gtrsim 60^\circ$  that flutter have similar equilibria and static stability properties as oriented flyers, though the torques tend to be amplified.

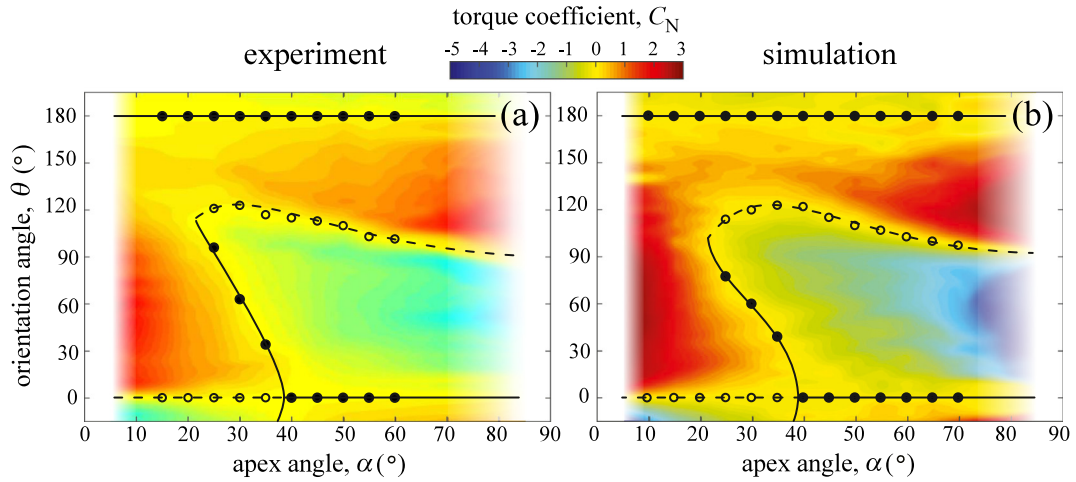


**Fig. 7.** Maps of the mean torque coefficient for wedges with half angle  $\alpha$  and orientation angle  $\theta$  for (a) experiments and (b) simulations. Markers indicate values of  $\alpha$  tested, and the maps are interpolated and extrapolated elsewhere. Filled markers and solid curves indicate stable equilibrium postures, and open symbols and dashed curves indicate unstable equilibria. (For interpretation of the references to color in this figure legend, the reader is referred to the web version of this article.)

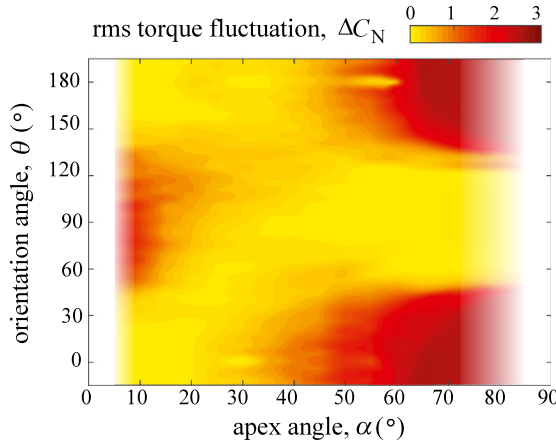


**Fig. 8.** Map of the fluctuating component of the torque from simulations. Root mean square (rms) fluctuations in the torque coefficient are displayed across wedges of half angle  $\alpha$  and orientation angle  $\theta$ . (For interpretation of the references to color in this figure legend, the reader is referred to the web version of this article.)

### 3.6. Maps of torque, fluctuations, equilibria and stability potential

How the torque depends on wedge shape and posture can be summarized by a colormap of  $C_N$  across half angles  $\alpha$  and orientation angles  $\theta$ . In Fig. 7 we display such maps from experiments and simulations. Equilibria arise when  $C_N = 0$  (yellow), and these conditions are indicated by the overlaid markers and curves. The markers denote the specific values of  $\alpha$  explored by each method, and the colormaps and connecting curves are interpolated and extrapolated elsewhere. The filled symbols and solid curves indicate orientations  $\theta$  inferred to be statically stable for a given  $\alpha$ , while the open markers and dashed curves indicate unstable postures.

The reported  $C_N$  represents the time average of the flow-induced torque, the instantaneous value of which can show significant fluctuations. To characterize these, we extract from simulations the root mean square of the torque  $\Delta N$ , which is normalized to form the fluctuation coefficient  $\Delta C_N = \frac{\Delta N}{\frac{1}{2}\rho U^2 A}$  and reported in the map of Fig. 8. These data show that fluctuations are highest (red) when a broad side of a body is presented to the flow, which occurs for narrow wedges aimed transversely ( $\alpha$  small and  $\theta \sim 90^\circ$ ) or broad wedges aimed either into or away from the flow ( $\alpha$  large and  $\theta \sim 0^\circ$  or  $180^\circ$ ). These fluctuations are closely linked to the build up and shedding of vorticity apparent in Fig. 3.

Another view of static stability involves the stability potential  $P$ , which is a dimensionless measure of the potential energy or work associated with rotation of a body away from  $\theta = 0^\circ$  given its torque profile (Amin et al., 2019):  $P(\alpha, \theta) = -\int_0^\theta C_N(\alpha, \theta') d\theta'$ . Here the torque-angle integral is the rotational analogue to the force-displacement integral

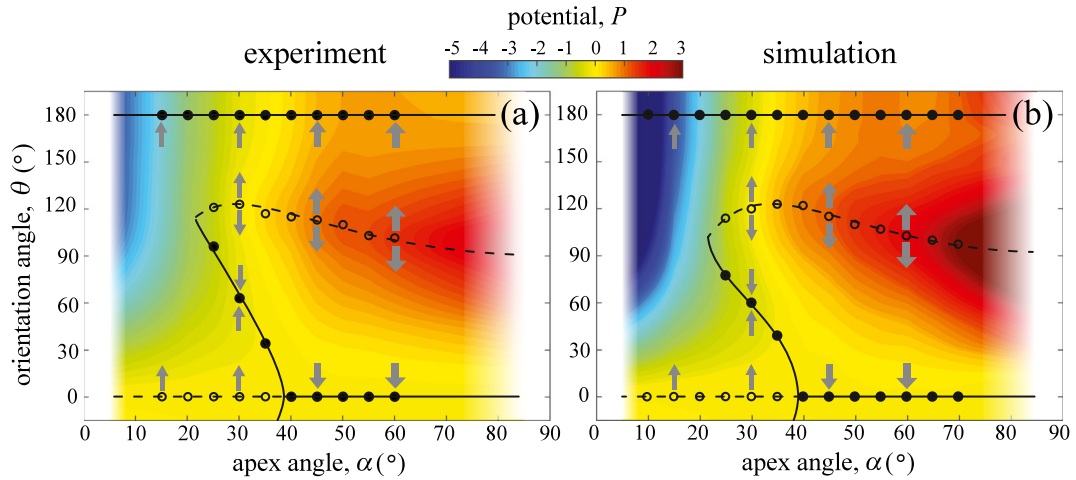


**Fig. 9.** Map of equilibrium orientation angles  $\theta$  and their stability across wedges of varying apex half angle  $\alpha$  for (a) experiments and (b) simulations. For each  $\alpha$ , the measured stable or attracting (filled markers) and unstable or repelling (open markers) orientation angles  $\theta$  are shown. The color map indicates the dimensionless stability potential  $P(\alpha, \theta) = -\int_0^\theta C_N(\alpha, \theta') d\theta'$ , which is computed for the marked  $\alpha$  values and interpolated and extrapolated elsewhere. (For interpretation of the references to color in this figure legend, the reader is referred to the web version of this article.)

representing work in translational systems. We calculate the potential profile across values of  $\alpha$ , and these data yield the maps shown in Figs. 9(a) and (b) for experiments and simulations, respectively. Markers indicate the values of  $\alpha$  at which measurements are performed, and the maps are interpolated and extrapolated elsewhere. Also shown are the equilibrium and stability curves. The map can be viewed as an energy landscape that dictates the orientation dynamics of each wedge  $\alpha$ : Bodies tend to evolve in  $\theta$  such that they ‘fall’ away from high values of  $P$  (warmer colors) and ‘down’ towards lower values (cooler colors). Stable orientations are local wells or valleys in the  $P$  landscape, and unstable equilibria are hilltops or ridges. Said another way, the stable points are attracting and the unstable points repelling, as indicated by the gray arrows.

For slender wedges of  $\alpha \lesssim 20^\circ$ , the minimum potential occurs at  $\theta = 180^\circ$ , which is consistent with their inversion in free flight. For somewhat broader wedges of  $25^\circ \lesssim \alpha \lesssim 35^\circ$ , the potential landscape is quite flat, which is consistent with these bodies showing no strong preference for any particular orientation and hence tumbling. For all broader wedges of  $\alpha \gtrsim 40^\circ$ , stable postures at  $\theta = 0^\circ$  and  $180^\circ$  correspond to low values of  $P$  separated by an unstable, high- $P$  ridge. The stably oriented flight or fluttering about  $\theta = 0^\circ$  of these bodies is consistent with the valley or well in the potential.

Viewed as a whole, the maps of the equilibria and their stability present an interesting structure that helps to understand the free flight behaviors. The curves of Figs. 9(a) and (b) connecting stable equilibria (solid) and unstable equilibria (dashed) reveal two critical points of bifurcations as  $\alpha$  is increased. Inverted fluttering gives way to tumbling via a blue-sky or saddle–node bifurcation near  $\alpha = 20^\circ$ , whereby a stable–unstable pair of equilibria is created. Tumbling then gives way to oriented flight via a pitchfork bifurcation near  $\alpha = 40^\circ$ , whereby the  $\theta = 0^\circ$  or apex-leading posture transforms from unstable to stable. The transition from oriented flight to fluttering near  $\alpha = 60^\circ$ , however, has no clear signature in these static stability maps, suggesting an inherently dynamical origin. Perhaps fluttering results from a destabilization of the  $\theta = 0^\circ$  posture excited by torque fluctuations, which are shown in Fig. 8 to strongly increase for  $\alpha \gtrsim 60^\circ$ .

### 3.7. Pressure field response to reorientation

Towards revealing mechanisms behind our static stability results, we use the simulations to assess the pressure field and especially the redistribution of pressure in response to misalignment to the flow. Pressure can be normalized by forming the instantaneous pressure coefficient  $C_p = \frac{p}{\frac{1}{2}\rho U^2}$ , a dimensionless form that incorporates high-Re pressure scaling with density  $\rho$  and flow speed  $U$ . In Figs. 10(a)–(d), we display the time-averaged pressure coefficients for wedges of half angles  $\alpha = 15^\circ, 30^\circ, 45^\circ$  and  $60^\circ$ , each oriented at  $\theta = 10^\circ$ . The color map is chosen such that positive pressures are indicated by warm colors and negative pressures by cool colors, and the particular wedges shown are representative of inverted fluttering, tumbling, oriented flight and fluttering.

While the overall pressures tend to be amplified with increasing  $\alpha$ , the fields show a number of common features across all wedges. The negative pressure in the wake region seems quite uniform over the downstream side in all cases. Since a symmetric or uniform back pressure would generate no torque about the center of mass, this suggests that the rear surface does not contribute significantly the torque response nor static stability. The pressure over the front faces shows stronger spatial variations, with the face that is more exposed to the oncoming flow taking on higher  $C_p$ . For  $\alpha = 15^\circ$ ,

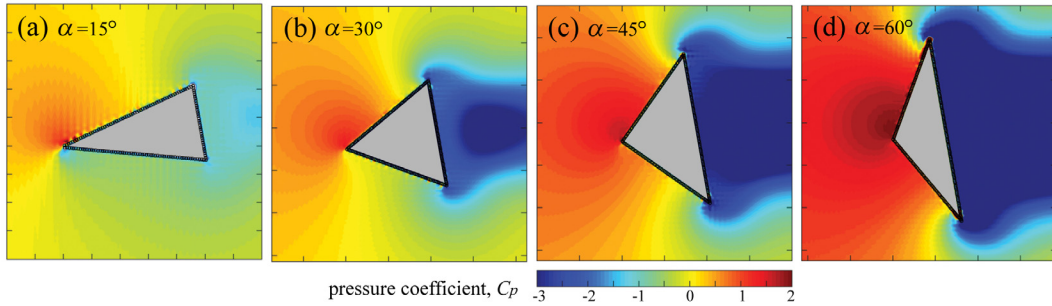


**Fig. 10.** Time-averaged pressure fields for wedges representing the free flight modes of (a) inverted fluttering, (b) tumbling, (c) oriented flight, and (d) fluttering. In each case, the body is oriented at  $\theta = 10^\circ$  relative to the incoming flow. (For interpretation of the references to color in this figure legend, the reader is referred to the web version of this article.)

the exposed face feels a high pressure that is concentrated near the apex, while the less exposed face is under a rather uniform negative pressure. Both of these traits would seem to contribute to destabilizing torques. Similar results hold for  $\alpha = 30^\circ$ , in which case the suction or negative pressure along the entire length of the less exposed face is somewhat surprising. For the broader bodies of  $\alpha = 45^\circ$  and  $\alpha = 60^\circ$ , the front pressure is more uniformly distributed with both faces largely under positive pressures. That high pressures extend further downstream along the more exposed face as compared to the less exposed face seems consistent with restorative torques and the static stability of these bodies.

#### 4. Discussion and conclusions

In this work, we report on experiments and simulations that reveal the flight modes and flight stability of solid triangular wedges or prisms. Quasi-2D free flight and water tunnel experiments at  $Re \approx 2000$  are compared to 2D immersed boundary simulations at  $Re \approx 200$ , and both methods show the same qualitative phenomena regarding stability of orientation. Specifically, the static stability or torque response to perturbations in orientation for wedges in imposed flows compare favorably for water tunnel experiments and forced-flow simulations. These results also help to interpret the dynamic stability and flight modes observed in experiments on wedges falling freely within water. To relate these aspects of this study, it is important to note that static stability is a necessary but not sufficient condition for dynamic stability. Torque measurements from both experiment and simulation show that the apex-leading orientation ( $\theta = 0^\circ$ ) is statically stable only for sufficiently broad wedges of apex half angle  $\alpha \gtrsim 40^\circ$ . Moreover, free flight experiments show that overly broad wedges  $\alpha \gtrsim 60^\circ$  experience a dynamic instability that manifests as fluttering or oscillations in orientation. Taken together, these results establish a range of wedge angles  $40^\circ \lesssim \alpha \lesssim 55^\circ$  that exhibit restorative torques and thus static stability, as well as the maintenance of oriented posture during free flight and thus dynamic stability.

These results can be summarized by the *Goldilocks rule*: Overly slender or sharp bodies lack static stability, overly broad or dull objects lack dynamic stability, and only intermediate bodies of the “just right” angularity achieve stably oriented flight. A right-angle triangle is a representative of these “just right” flyers, and we show that moderate perturbations to this shape do not undermine its stability. The stability is also preserved for the somewhat different values of Reynolds numbers explored in experiments and simulations. The general rule holds for 3D-axisymmetric bodies, *i.e.* the family of cones studied previously (Amin et al., 2019), as well as 2D bodies, *i.e.* the family of wedges reported here. Remarkably, the class of meteorites that are thought to have maintained oriented flight as meteoroids in the atmosphere also resemble cones of intermediate apex angles (Amin et al., 2019), a curious correspondence given the vastly different regime of hypersonic flight. In light of all these findings, it seems the rule may be quite universal and thus generally useful when reasoning about the flight stability of objects.

Future work should assess dynamic stability through free fall simulations and observation of flight modes across values of  $\alpha$ . More investigation is also needed to understand the motion-posture couplings during flight and the mechanisms behind the observed changes in stability with body shape. Static stability simulations of the kind reported here would seem to be the most informative route towards a more quantitative understanding of how pressure is redistributed to produce restoring (stabilizing) or amplifying (destabilizing) torques. Why “just right” wedges and cones are dynamically stable, and how postural perturbations are stably damped, also await future studies. Similarly, the origin of the dynamic instability of overly broad bodies, and what excites their fluttering oscillations, remain to be explained. These aspects will likely involve inherently unsteady phenomena such as added mass effects and vortex shedding.

The general problem of the flight stability of wedge shapes involves three dimensionless parameters (Ern et al., 2012): the half angle  $\alpha$ , Reynolds number  $Re$ , and either the solid-to-fluid density ratio or a corresponding ratio of moments of inertia. Our study spans  $\alpha$  but explores a limited range of  $Re \approx 200$  to 2000. Future work might consider  $Re < 10^2$ , where viscous effects become increasingly important, as well as  $Re > 10^4$ , for which the near-body flows are increasingly susceptible to turbulence. Regarding the third dimensionless parameter, studies of the free flight modes of thin plates

and disks indicate the importance of the solid moment of inertia (Willmarth et al., 1964; Smith, 1971; Field et al., 1997; Andersen et al., 2005), which may be made dimensionless by scaling on a corresponding moment of the surrounding fluid. In particular, increasing the dimensionless moment tends to drive the transition from fluttering to tumbling. Because our free flight experiments consider triangular prisms whose cross-section area  $A$ , depth in the third dimension, and mass  $M$  are all fixed constants, the solid moment of inertia about the center of mass depends on  $\alpha$ :  $I = \frac{1}{6}MA [\tan \alpha + 1/(3 \tan \alpha)]$ , which displays a broad minimum at  $\alpha = 30^\circ$  and increases strongly at very low and very high  $\alpha$ . However, for the range  $\alpha \in [15^\circ, 60^\circ]$  spanning the four observed flight modes, the moment changes only by about 50%. Further, our results show that wedges that tumble have low  $I$  while those that display one of the two fluttering modes have higher  $I$ , which is counter to the trend seen for plates and disks. For these reasons, we interpret the transitions in flight behavior of wedges observed here as primarily driven by the wedge shape, as quantified by  $\alpha$ , rather than by the moment of inertia. This claim could be tested by systematic characterization of the flight modes across the space of the three dimensionless parameters.

### CRediT authorship contribution statement

**Pejman Sanaei:** Designed the study, Data analysis, Composition of the manuscript. **Guanhua Sun:** Implemented and carried out the simulations, Data analysis, Composition of the manuscript. **Huilin Li:** Carried out the experiments, Data analysis, Composition of the manuscript. **Charles S. Peskin:** Designed the study, Implemented and carried out the simulations, Data analysis, Composition of the manuscript. **Leif Ristroph:** Designed the study, Carried out the experiments, Data analysis, Composition of the manuscript.

### Declaration of competing interest

The authors declare that they have no known competing financial interests or personal relationships that could have appeared to influence the work reported in this paper.

### Acknowledgments

The authors gratefully acknowledge an NSF Research and Training Grant, United States of America (RTG, DMS-1646339) awarded to CP and LR and supporting PS with postdoctoral support, as well as the NSF grant CBET-1805506 to LR. PS also acknowledges an Institutional Support of Research and Creativity (ISRC) grant provided by New York Institute of Technology, United States of America. GS and HL were supported by New York University, United States of America and NYU-Shanghai, China through the SURE and DURF programs.

### References

- Abzug, M.J., Larrabee, E., 2005. *Airplane Stability and Control: A History of the Technologies that Made Aviation Possible*, Vol. 14. Cambridge University Press.
- Acrivos, A., Leal, L., Snowden, D., Pan, F., 1968. Further experiments on steady separated flows past bluff objects. *J. Fluid Mech.* 34 (1), 25–48.
- Alben, S., Shelley, M., Zhang, J., 2002. Drag reduction through self-similar bending of a flexible body. *Nature* 420 (6915), 479.
- Amin, K., Mac Huang, J., Hu, K.J., Zhang, J., Ristroph, L., 2019. The role of shape-dependent flight stability in the origin of oriented meteorites. *Proc. Natl. Acad. Sci.* 116 (33), 16180–16185.
- Andersen, A., Pesavento, U., Wang, Z.J., 2005. Unsteady aerodynamics of fluttering and tumbling plates. *J. Fluid Mech.* 541, 65–90.
- Arthurs, K.M., Moore, L.C., Peskin, C.S., Pitman, E.B., Layton, H., 1998. Modeling arteriolar flow and mass transport using the immersed boundary method. *J. Comput. Phys.* 147 (2), 402–440.
- Balboa, F., Bell, J., Delgado-Buscallioni, R., Donev, A., Fai, T., Griffith, B., Peskin, C., 2011. Staggered schemes for incompressible fluctuating hydrodynamics.
- Camari, S., Salvetti, M.V., Buresti, G., 2006. Large-eddy simulation of the flow around a triangular prism with moderate aspect ratio. *J. Wind Eng. Ind. Aerodyn.* 94 (5), 309–322.
- Devendran, D., Peskin, C.S., 2012. An immersed boundary energy-based method for incompressible viscoelasticity. *J. Comput. Phys.* 231 (14), 4613–4642.
- El-Sherbiny, S., 1983. Flow separation and reattachment over the sides of a 90 triangular prism. *J. Wind Eng. Ind. Aerodyn.* 11 (1–3), 393–403.
- Ern, P., Risso, F., Fabre, D., Magnaudet, J., 2012. Wake-induced oscillatory paths of bodies freely rising or falling in fluids. *Annu. Rev. Fluid Mech.* 44, 97–121.
- Field, S.B., Klaus, M., Moore, M., Nori, F., 1997. Chaotic dynamics of falling disks. *Nature* 388 (6639), 252.
- Griffith, B.E., Luo, X., McQueen, D.M., Peskin, C.S., 2009. Simulating the fluid dynamics of natural and prosthetic heart valves using the immersed boundary method. *Int. J. Appl. Mech.* 1 (01), 137–177.
- IBAMR: An Adaptive and distributed-memory parallel implementation of the immersed boundary method, <https://github.com/IBAMR/IBAMR>.
- Jayaweera, K., Mason, B., 1965. The behaviour of freely falling cylinders and cones in a viscous fluid. *J. Fluid Mech.* 22 (4), 709–720.
- Kim, J.-T., Jin, Y., Shen, S., Dash, A., Chamorro, L.P., 2020. Free fall of homogeneous and heterogeneous cones. *Phys. Rev. Fluids* 5 (9), 093801.
- Kim, Y., Peskin, C.S., 2006. 2-D parachute simulation by the immersed boundary method. *SIAM J. Sci. Comput.* 28 (6), 2294–2312.
- Kim, Y., Peskin, C.S., 2009. 3-D parachute simulation by the immersed boundary method. *Comput. & Fluids* 38 (6), 1080–1090.
- Kim, Y., Peskin, C.S., 2016. A penalty immersed boundary method for a rigid body in fluid. *Phys. Fluids* 28 (3), 033603.
- Kumar De, A., Dalal, A., 2006. Numerical simulation of unconfined flow past a triangular cylinder. *Internat. J. Numer. Methods Fluids* 52 (7), 801–821.
- Lai, M.-C., Peskin, C.S., 2000. An immersed boundary method with formal second-order accuracy and reduced numerical viscosity. *J. Comput. Phys.* 160 (2), 705–719.
- Liepmann, H.W., Bryson, Jr., A., 1950. Transonic flow past wedge sections. *J. Aeronaut. Sci.* 17 (12), 745–755.

- Lorenz, R.D., 2007. *Spinning Flight: Dynamics of Frisbees, Boomerangs, Samaras, and Skipping Stones*. Springer Science & Business Media.
- McQueen, D., Peskin, C., 1997. Shared-memory parallel vector implementation of the immersed boundary method for the computation of blood flow in the beating mammalian heart. *J. Supercomput.* 11 (3), 213–236.
- Moore, M.N., Ristroph, L., Childress, S., Zhang, J., Shelley, M.J., 2013. Self-similar evolution of a body eroding in a fluid flow. *Phys. Fluids* 25 (11), 116602.
- Murphy, C.H., 1981. Symmetric missile dynamic instabilities. *J. Guid. Control* 4 (5), 464–471.
- Norton, O.R., 2002. *The Cambridge encyclopedia of meteorites*.
- Pesavento, U., Wang, Z.J., 2004. Falling paper: Navier–Stokes solutions, model of fluid forces, and center of mass elevation. *Phys. Rev. Lett.* 93 (14), 144501.
- Peskin, C.S., 1972. Flow patterns around heart valves: a numerical method. *J. Comput. Phys.* 10 (2), 252–271.
- Prasath, S.G., Sudharsan, M., Kumar, V.V., Diwakar, S., Sundararajan, T., Tiwari, S., 2014. Effects of aspect ratio and orientation on the wake characteristics of low Reynolds number flow over a triangular prism. *J. Fluids Struct.* 46, 59–76.
- Ristroph, L., Moore, M.N., Childress, S., Shelley, M.J., Zhang, J., 2012. Sculpting of an erodible body by flowing water. *Proc. Natl. Acad. Sci.* 109 (48), 19606–19609.
- Ristroph, L., Zhang, J., 2008. Anomalous hydrodynamic drafting of interacting flapping flags. *Phys. Rev. Lett.* 101 (19), 194502.
- Schlichting, H., Gersten, K., 2016. *Boundary-layer Theory*. Springer.
- Skews, B., 1991. Autorotation of many-sided bodies in an airstream. *Nature* 352 (6335), 512–513.
- Smith, E., 1971. Autorotating wings: an experimental investigation. *J. Fluid Mech.* 50 (3), 513–534.
- Tatsuno, M., Takayama, T., Amamoto, H., Ishi-i, K., 1990. On the stable posture of a triangular or a square cylinder about its central axis in a uniform flow. *Fluid Dyn. Res.* 6 (3–4), 201–207.
- Tritton, D.J., 2012. *Physical Fluid Dynamics*. Springer Science & Business Media.
- Wang, S., Zhu, L., Zhang, X., He, G., 2011. Flow past two freely rotatable triangular cylinders in tandem arrangement. *J. Fluids Eng.* 133 (8), 081202.
- Willmarth, W.W., Hawk, N.E., Harvey, R.L., 1964. Steady and unsteady motions and wakes of freely falling disks. *Phys. Fluids* 7 (2), 197–208.